Figure 5. Stellar mass completeness of the sample, divided into three fields depending on exposure time (T_{exp}). The larger grey circles show the stellar mass of each galaxy as a function of redshift, while the smaller coloured circles show the limiting mass for the faintest 20 per cent. The solid curves denote the 90 per cent completeness at each redshift and for each depth, as indicated in the legend, following the prescription of Pozzetti et al. (2010). We find our sample is stellar mass complete down to $\log(M_\star/[M_\odot]) \approx 7.5$, with small variations depending on the depth of the field. The dotted vertical lines mark the redshift bins used in the mass completeness estimation, while the numbers provided in each bin indicate the total number of galaxies in the bin (top row, bold faced), and the galaxies above the limiting mass (bottom row, in brackets).

circles), the coloured small circles show the M_{lim} of the faintest 20 per cent of galaxies for each field, and the filled lines denote the 90 per cent completeness as a function of redshift. We find that, in general, our photometric sample is stellar mass complete down to $\log(M_\star/[M_\odot]) \approx 7.5$, with slight variations depending on the depth of the observations (within ~ 0.2 dex).

In the remainder of this study, we focus only on sources that have a PROSPECTOR-derived stellar mass with a median above the mass completeness limit ($\log(M_\star/[M_\odot]) \approx 7.5$), yielding a sample of 14 652 galaxies, which are UV complete down to $M_{UV} \approx -16$.

4.3 M_{UV}–$M_\star$ relation

Fig. 6 shows the stellar mass of our stellar mass complete sample as a function of M_{UV}, divided by redshift bins. The numbers on the top of each panel indicate the number of galaxies in any given bin. We fit the observational data in the M_{UV}–$M_\star$ plane taking into account the completeness limits discussed in the previous section. Specifically, we fit the following relation

$$\log(M_\star) = \alpha(M_{UV} + 19.5) + \log(M_{\star,0}), \qquad (2)$$

where $M_\star$ is stellar mass in units of solar masses, α is the slope of the M_{UV}–$M_\star$ relation and $\log(M_{\star,0})$ is its normalization (stellar mass at $M_{UV} = -19.5$ AB mag). In addition to these two parameters, we also fit for the scatter $\sigma_{M_{UV}-M_\star}$ in M_{UV} at fixed $M_\star$. We then fit these three parameters to the observed distribution using the dynamic nested sampling code DYNESTY (Speagle 2020). In each model call, we sample the M_{UV}–$M_\star$ relation (with scatter) with 1 million galaxies assuming an M_{UV} that follows the UV luminosity function (Bouwens et al. 2021), bin this drawn galaxy sample in the M_{UV}–$M_\star$ plane taking into account the completeness limits, and

compare the normalized histogram with the observed one. The best-fitting parameters can be found in Table 1, for the highest redshift bin ($8 < z \leq 9$) we adopt the best-fitting results from the previous redshift bin ($7 < z \leq 8$).

From the nearly linear relation between $\log(M_\star)$ and $\log(SFR)$ (i.e. star-forming main sequence; Brinchmann et al. 2004; Daddi et al. 2007; Salim et al. 2007), we would expect a slope α of the M_{UV}–$M_\star$ relation close to -0.4, assuming a simple, linear conversion between the UV luminosity and SFR (Kennicutt 1998; Madau, Pozzetti & Dickinson 1998; Salim et al. 2007). Our steeper slope of ≈ -0.6 is consistent with having a higher mass-to-light ratio ($M_\star/L_{UV}$) for more massive systems, in agreement with the findings of González et al. (2011). We further find that $\log(M_{\star,0})$ decreases with increasing redshift ($M_{\star,0} \propto (1+z)^{-2.7}$), i.e. at fixed $M_{UV} = -19.5$ the typical stellar mass of the galaxies is lower at earlier cosmic times. This implies a lower $M_\star/L_{UV}$ toward higher redshifts, consistent with younger stellar populations toward earlier times. A combination of less dust attenuation and higher specific SFR toward higher redshifts and at fixed stellar mass could lead to this outcome. Finally, the scatter of the M_{UV}–$M_\star$ relation is substantial with 0.6–0.7 dex. This scatter includes both the intrinsic scatter of the M_{UV}–$M_\star$ relation and the observational uncertainty, though the latter is only of the order of 0.2 dex.

As comparison, we show the $\log(M_\star)$–M_{UV} mass-to-light relations from Duncan et al. (2014), Song et al. (2016), and Tacchella et al. (2018). The Duncan et al. (2014) and Song et al. (2016) relations are derived from a combination of observations (i.e. *Spitzer*/IRAC and *HST*) and SED fitting, while the one from Tacchella et al. (2018) is based on an empirical model that links star formation in galaxies to the accretion rate of dark matter halos. With our stellar mass complete sample, we find a somewhat steeper slope than previous observational studies (but mostly $< 1\sigma$ discrepant; ~ -0.6 instead of ~ -0.4 to -0.5). This effect is partly a consequence of our sample including a larger population of fainter sources (with lower stellar masses) than the mentioned studies, but also because we consider explicitly the mass completeness of our sample. Specifically, we forward model the completeness when fitting the relation; if we do not do that, we find a shallower relation of ~ -0.4. Additionally, the stellar masses in these previous studies were estimated assuming parametric SFHs, which cannot fully describe the complexities of galaxies (Lower et al. 2020), while we assume more flexible SFHs.

5 CONSTRAINTS ON THE IONIZING PROPERTIES OF GALAXIES

In this section, we provide a brief overview of the methods traditionally used to infer ionizing properties of galaxies. Followed by the trends of ξ_{ion} and $\dot{n}_{ion}$ with redshift and UV magnitude, including a comparison with values from the literature. Finally, we discuss the emergence of a secondary (previously unseen) sample of galaxies, that are tentatively leaking Ly C. An excerpt of the properties used in this section is given in Table 2.

5.1 Measuring ξ_{ion} from emission line fluxes

The ionizing photon production efficiency, ξ_{ion}, can be measured through Hα and/or [O III] emission line fluxes. In order to use Hα as a proxy for ionizing photon production efficiency (ξ_{ion}), one must first correct the Hα line flux for dust (for example, using an SMC attenuation curve; Gordon et al. 2003). If Case B recombination is assumed, along with the assumption of no Ly C f_{esc}, and that dust has a negligible effect on Ly C photons, the dust corrected
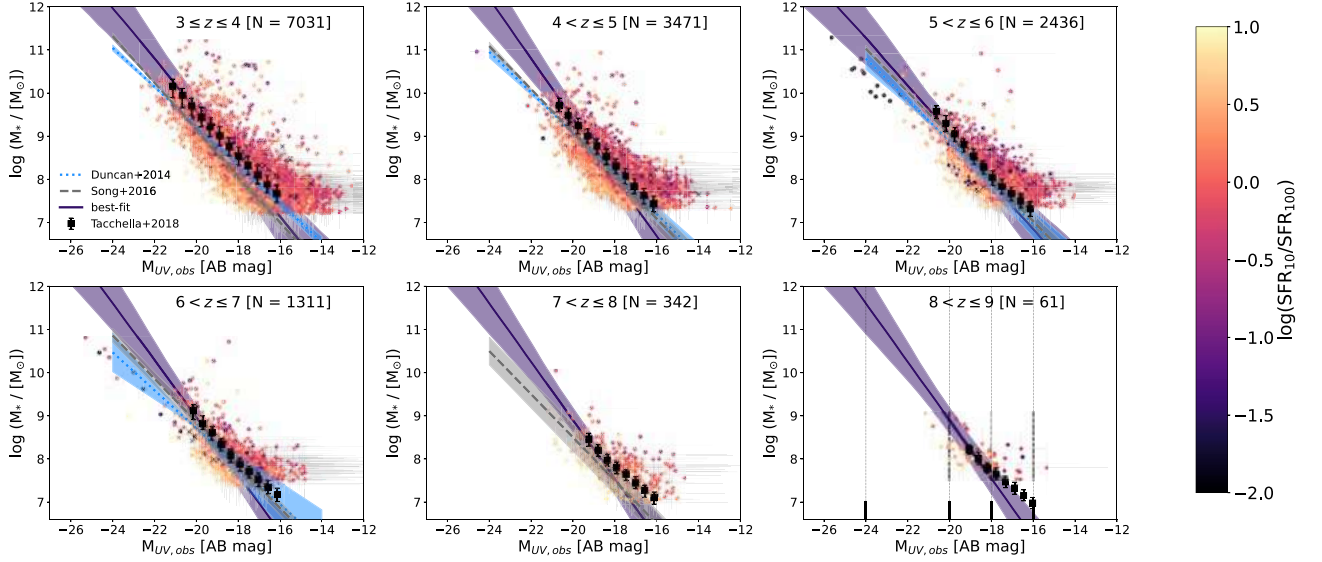
Figure 6. Stellar mass as a function of (observed) M_{UV} for our stellar mass complete sample, divided into redshift bins, and colour-coded by the burstiness of their SFHs (i.e. ratio between star formation in the past 10 Myr and the one averaged over the last 100 Myr). For comparison, we overlay the $\log(M_\star)$–M_{UV} mass-to-light relations from Duncan et al. (2014), Song et al. (2016), and Tacchella et al. (2018). The best-fitting relation, using forward modelling to take account for the completeness of the sample, is shown as a purple solid curve and shaded area (see Table 1). The black vertical lines in the bottom right panel show the limits of three M_{UV} bins delimited by $M_{UV} = -24$, -20, -18, and -16, which are used later in Fig. 16. As expected, brighter galaxies tend to have higher stellar masses, however, there is a considerable scatter in M_{UV} for a fixed stellar mass.

Table 1. Best-fitting parameters for $\log(M_\star)$–M_{UV} relation as parametrized by equation (2). *Column 1:* redshift bin. *Column 2:* slope of the relation. *Column 3:* stellar mass normalization ($\log(M_\star)$ at $M_{UV} = -19.5$. *Column 4:* scatter in $\log(M_\star)$ at fixed M_{UV}.

Redshift	α	$\log(M_{\star,0}/[M_\odot])$	σ [dex]
$3 \leq z \leq 4$	$-0.60^{+0.27}_{-0.33}$	$9.25^{+0.77}_{-0.71}$	$0.66^{+0.31}_{-0.28}$
$4 < z \leq 5$	$-0.69^{+0.26}_{-0.28}$	$9.06^{+0.62}_{-0.63}$	$0.69^{+0.29}_{-0.28}$
$5 < z \leq 6$	$-0.55^{+0.20}_{-0.32}$	$8.78^{+0.71}_{-0.60}$	$0.57^{+0.37}_{-0.22}$
$6 < z \leq 7$	$-0.65^{+0.21}_{-0.30}$	$8.63^{+0.51}_{-0.46}$	$0.56^{+0.37}_{-0.21}$
$7 < z \leq 8$	$-0.68^{+0.25}_{-0.28}$	$8.55^{+0.57}_{-0.57}$	$0.72^{+0.26}_{-0.26}$

H α luminosity relates directly to the rate of ionizing photons ($\dot{n}_{ion}$, in units of s^{-1}) that are being emitted ($\dot{n}_{ion} = 7.28 \times 10^{11}$ L(H α); Osterbrock & Ferland 2006). ξ_{ion} is then the ratio between $\dot{n}_{ion}$ and the observed monochromatic UV luminosity density (measured at rest-frame $\lambda = 1500$ Å). This method suffers from a number of assumptions that need to be made: it has a great dependence on the chosen attenuation curve, and Case B recombination cannot always be assumed (McClymont et al. 2024; Scarlata et al. 2024). If [O III]$_{\lambda 5007}$ is available instead, its equivalent width can give a measure of the ionization field of the galaxy as shown in Chevallard et al. (2018), and later in Tang et al. (2019). This method also depends on the shape of the attenuation curve assumed, as well as on the gas-phase metallicity and nebular conditions.

In Simmonds et al. (2024a), the ionizing properties of a sample of 677 emission line galaxies at $z \sim 4 - 9$ were analysed. These galaxies had signatures of either H α and/or [O III] emission in their NIRCam photometry, specifically with a 5σ detection in the filter pairs F335M–F356W and F410M–F444W. Both methods mentioned above were used to estimate ξ_{ion}, while in parallel, PROSPECTOR was used to fit their full NIRCam photometry (assuming $f_{esc} = 0$). A tight

agreement was found between the values measured by emission line fluxes and those inferred by PROSPECTOR. Therefore, in this work we rely on this SED fitting code to extract the ionizing properties of a stellar mass complete sample, allowing us to potentially study all types of galaxies, not only those with detectable emission lines. Since our PROSPECTOR fitting routine assumes an escape fraction of zero, our estimated ionizing photon production efficiencies ($\xi_{ion,0}$) include a correcting factor of $1 - f_{esc}$, such that:

$$\xi_{ion,0} = \xi_{ion} \times (1 - f_{esc}). \tag{3}$$

Appendix C shows how well PROSPECTOR can constrain stellar masses and ionizing photon production efficiencies, as a function of flux in F444W.

5.2 Trends of ionizing properties with redshift

We first compare our results to those from the literature, in particular, for the evolution of $\xi_{ion,0}$ with redshift. Fig. 7 encodes most results to date. Stefanon et al. (2022) compiled $\xi_{ion,0}$ measurements up to $z \sim 8$ (containing data from Stark et al. 2015; Bouwens et al. 2016; Mármol-Queraltó et al. 2016; Nakajima et al. 2016; Matthee et al. 2017; Stark et al. 2017; Harikane et al. 2018; Shivaei et al. 2018; De Barros et al. 2019; Faisst et al. 2019; Lam et al. 2019; Tang et al. 2019; Emami et al. 2020; Nanayakkara et al. 2020; Endsley et al. 2021; Atek et al. 2022; Naidu et al. 2022). This extensive compilation allowed them to estimate the rate of change of $\xi_{ion,0}$ with redshift, finding it to have a slope of $d\log(\xi_{ion,0})/dz = 0.09 \pm 0.01$ (black dashed line). The markers show the UV-faint galaxies at $z \sim 3-7$ from Prieto-Lyon et al. (2023), the Lyman-α emitters (LAEs) from Ning et al. (2023) and Simmonds et al. (2023), the H α emitters from Rinaldi et al. (2024), and the ELGs from Simmonds et al. (2024a). The latter show a slightly less steep evolution of $\xi_{ion,0}$ with redshift than the compilation of Stefanon et al. (2022), but consistent within errors [given by $d\log(\xi_{ion,0})/dz = 0.07 \pm 0.02$]. Finally, the stellar

Table 2. Table excerpt of general properties for a selection of galaxies studied in this work. *Column 1:* JADES identifier, composed of the coordinates of the centroid rounded to the fifth decimal place, in units of degrees. *Column 2:* photometric redshift inferred using the SED fitting code PROSPECTOR. *Column 3:* logarithm of stellar mass. *Column 4:* logarithm of the ionizing photon production efficiency. *Column 5:* logarithm of the rate of ionizing photons being emitted. *Column 6:* logarithm of the burstiness of SFH, defined as the ratio between recent star formation (<10 Myr) and the one averaged over the past 100 Myr (using the median values of SFR_{10} and SFR_{100}). *Column 7:* observed UV magnitude.

| Name	z	$\log(M)$ [$M_\odot$]	$\log(\xi_{ion,0})$ [Hz erg^{-1}]	$\log(\dot{n}_{ion})$ [s^{-1}]	$\log(SFR_{10}/SFR_{100})$	$M_{UV,obs}$ [AB]
JADES-GS+53.14866−27.77800	$3.31^{+0.19}_{-0.07}$	$7.85^{+0.07}_{-0.14}$	$25.23^{+0.25}_{-0.10}$	$53.03^{+0.19}_{-0.30}$	0.04	$-14.65^{+0.88}_{-0.54}$
JADES-GS+53.12095−27.87018	$3.33^{+0.10}_{-0.07}$	$8.08^{+0.09}_{-0.14}$	$25.37^{+0.13}_{-0.08}$	$53.43^{+0.19}_{-0.21}$	-0.13	$-17.39^{+0.25}_{-0.11}$
JADES-GS+53.11867−27.78184	$3.74^{+0.02}_{-0.12}$	$7.93^{+0.13}_{-0.19}$	$25.27^{+0.27}_{-0.21}$	$53.07^{+0.27}_{-0.16}$	0.05	$-17.51^{+0.08}_{-0.08}$
JADES-GS+53.08300−27.72764	$3.13^{+0.20}_{-0.24}$	$8.23^{+0.16}_{-0.23}$	$25.28^{+0.18}_{-0.24}$	$52.93^{+0.19}_{-0.19}$	-0.07	$-16.60^{+0.36}_{-0.30}$
JADES-GS+53.04080−27.92276	$3.22^{+0.21}_{-0.38}$	$8.30^{+0.11}_{-0.17}$	$25.30^{+0.17}_{-0.25}$	$52.95^{+0.19}_{-0.25}$	-0.02	$-16.89^{+0.49}_{-0.30}$
JADES-GS+53.09258−27.82776	$3.10^{+0.05}_{-0.03}$	$9.01^{+0.11}_{-0.17}$	$25.35^{+0.07}_{-0.10}$	$53.90^{+0.18}_{-0.17}$	0.30	$-18.25^{+0.14}_{-0.11}$
JADES-GS+53.12590−27.74766	$3.99^{+1.71}_{-0.10}$	$7.76^{+0.28}_{-0.22}$	$25.36^{+0.10}_{-0.16}$	$52.91^{+0.46}_{-0.19}$	0.11	$-16.76^{+0.34}_{-0.72}$
JADES-GS+53.13889−27.88894	$3.36^{+0.06}_{-0.15}$	$7.61^{+0.18}_{-0.28}$	$25.57^{+0.08}_{-0.04}$	$53.43^{+0.13}_{-0.24}$	0.46	$-16.04^{+0.40}_{-0.25}$
JADES-GS+53.22062−27.80017	$3.51^{+0.19}_{-0.39}$	$8.13^{+0.18}_{-0.35}$	$25.32^{+0.19}_{-0.31}$	$53.00^{+0.33}_{-0.56}$	0.02	$-16.61^{+0.77}_{-0.44}$
JADES-GS+53.10416−27.76468	$3.22^{+0.43}_{-0.55}$	$7.91^{+0.15}_{-0.25}$	$25.16^{+0.29}_{-0.62}$	$52.18^{+0.60}_{-0.93}$	-0.15	$-14.52^{+1.45}_{-0.99}$
JADES-GS+53.10666−27.85285	$3.70^{+0.06}_{-0.01}$	$8.69^{+0.25}_{-0.05}$	$25.34^{+0.12}_{-0.18}$	$54.11^{+0.11}_{-0.05}$	0.23	$-19.37^{+0.05}_{-0.05}$
JADES-GS+53.14954−27.83692	$3.47^{+0.18}_{-0.20}$	$8.44^{+0.07}_{-0.17}$	$24.71^{+0.38}_{-0.62}$	$52.42^{+0.39}_{-0.59}$	-0.69	$-17.37^{+0.25}_{-0.16}$
JADES-GS+53.13434−27.87952	$3.63^{+0.06}_{-0.10}$	$9.23^{+0.08}_{-0.55}$	$25.20^{+0.17}_{-0.20}$	$54.20^{+0.13}_{-0.23}$	0.06	$-19.42^{+0.06}_{-0.07}$
JADES-GS+53.07363−27.80199	$3.79^{+0.16}_{-0.09}$	$8.21^{+0.13}_{-0.16}$	$25.06^{+0.29}_{-0.39}$	$52.51^{+0.38}_{-0.43}$	-0.30	$-16.48^{+0.29}_{-0.24}$
JADES-GS+53.11274−27.86907	$3.57^{+0.20}_{-0.55}$	$7.77^{+0.15}_{-0.25}$	$25.27^{+0.20}_{-0.34}$	$52.46^{+0.34}_{-0.46}$	-0.15	$-15.69^{+0.59}_{-0.46}$
JADES-GS+53.06192−27.71806	$3.09^{+0.04}_{-0.02}$	$8.01^{+0.04}_{-0.07}$	$25.45^{+0.16}_{-0.02}$	$53.76^{+0.09}_{-0.14}$	0.50	$-16.01^{+0.57}_{-0.12}$
JADES-GS+53.11460−27.77632	$3.70^{+2.91}_{-0.27}$	$7.87^{+0.10}_{-0.28}$	$25.54^{+0.12}_{-0.19}$	$53.18^{+0.98}_{-0.39}$	0.26	$-15.97^{+0.82}_{-1.26}$
JADES-GS+53.12350−27.89819	$3.06^{+0.10}_{-0.25}$	$8.51^{+0.14}_{-0.20}$	$25.24^{+0.15}_{-0.52}$	$53.22^{+0.25}_{-0.46}$	-0.09	$-18.00^{+0.19}_{-0.13}$
JADES-GS+53.11707−27.76709	$3.09^{+0.03}_{-0.02}$	$7.79^{+0.15}_{-0.38}$	$25.49^{+0.08}_{-0.08}$	$53.02^{+0.34}_{-0.24}$	0.33	$-15.56^{+0.50}_{-0.25}$
JADES-GS+53.09145−27.91365	$3.51^{+0.14}_{-0.18}$	$8.26^{+0.17}_{-0.29}$	$25.24^{+0.14}_{-0.27}$	$52.95^{+0.24}_{-0.29}$	-0.10	$-17.28^{+0.18}_{-0.19}$
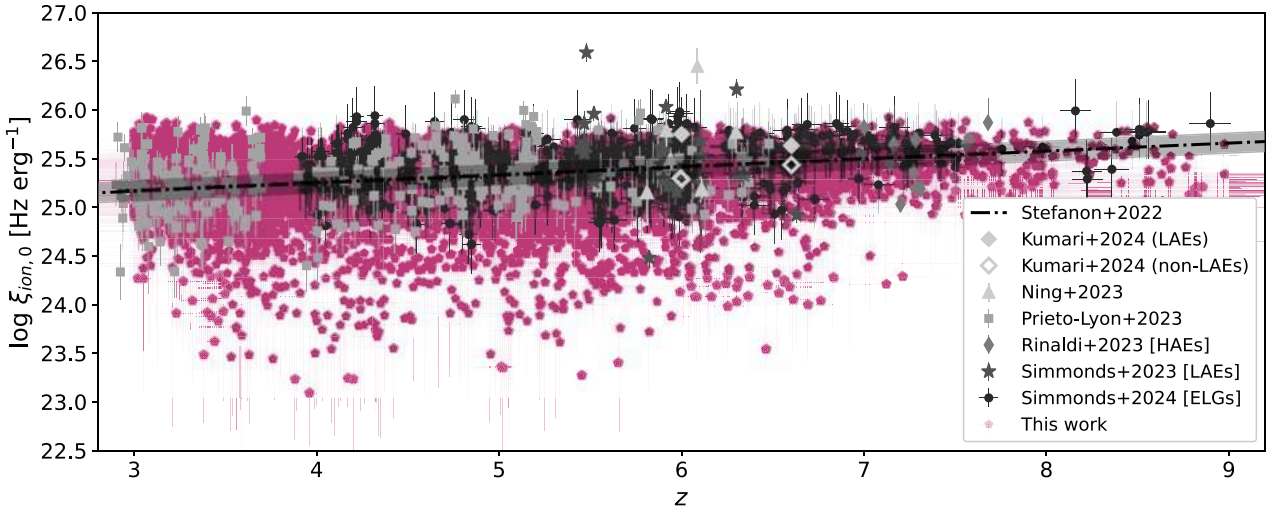
Figure 7. Compilation of $\xi_{ion,0}$ from literature, in comparison to our stellar mass complete sample (this work, pentagons). The best-fitting line from Stefanon et al. (2022), with a slope of $d\log(\xi_{ion,0})/dz = 0.09 \pm 0.01$, is shown as a black dashed line and shaded area. In order of increasing redshift, the markers in grey scale represent: UV-faint galaxies at $z \sim 3$–7 from Prieto-Lyon et al. (2023) (squares), Lyα emitters from Ning et al. (2023) (triangles) and Simmonds et al. (2023) (stars), the Hα emitters from Rinaldi et al. (2024) (thin diamonds), and finally, the ELGs from Simmonds et al. (2024a), which have a slope of $d\log(\xi_{ion,0})/dz = 0.07 \pm 0.02$. The thick diamonds show the stacked results from Kumari et al. (2024), for galaxies above and below $z = 6.3$. Due to observational limitations and the emission line methods used to estimate $\xi_{ion,0}$ (i.e. through Hα and/or [O III] emission) the previous samples were biased towards star-forming galaxies. Our stellar mass complete sample reveals a population of galaxies with low-ionizing photon production efficiency ($\log(\xi_{ion,0}/[\text{Hz erg}^{-1}]) \lesssim 24.5$), and a considerably less significant evolution with redshift ($d\log(\xi_{ion,0})/dz \sim 0.01$, see Fig. 8).